THE ASTROPHYSICAL JOURNAL, 518:676–692, 1999 June 20

THE LOCATION OF THE NUCLEUS OF NGC 1068 AND THE THREE-DIMENSIONAL STRUCTURE OF ITS NUCLEAR REGION[1]

MAKOTO KISHIMOTO
Department of Astronomy, Faculty of Science, Kyoto University, Sakyo-ku, Kyoto 606-8502, Japan
Received 1998 April 15; accepted 1999 January 27

ABSTRACT

The *Hubble Space Telescope* (*HST*) archival UV imaging polarimetry data of NGC 1068 are re-examined. Through an extensive estimation of the observational errors, we discuss whether the distribution of the position angles (P.A.s) of polarization is simply centrosymmetric or not. Taking into account the effect of a bad focus at the time of the observation, we conclude that, within the accuracy of *HST*/FOC polarimetry, the P.A. distribution is completely centrosymmetric. This means that the UV polarization originates only from scattering of the radiation from a central pointlike source. However, our analysis shows that the most probable location of the nucleus is only $\sim 0\farcs08$ (~ 6 pc) south from the brightest cloud called cloud B. The error circle of 99% confidence level extends to cloud B and to cloud A, which is about $0\farcs2$ south of cloud B. By this FOC observation, cloud B is only marginally rejected as the nucleus. Assuming that the UV flux is dominated by electron-scattered light, we have also derived a three-dimensional structure of the nuclear region. The inferred distribution suggests a linear structure that could be related to the radio jet.

Subject headings: galaxies: individual (NGC 1068) — galaxies: Seyfert — galaxies: structure — ISM: clouds — polarization — scattering

1. INTRODUCTION

The nucleus of the Seyfert 2 galaxy NGC 1068 is now firmly believed to be obscured from direct view. This was clearly inferred by Antonucci & Miller (1985) from a spectropolarimetric study, and now one of the major problems in this galaxy is to locate this hidden nucleus very accurately on the high-resolution images taken by the *Hubble Space Telescope* (*HST*) and on VLBI radio maps. This is particularly important, since the investigation of the physical conditions and kinematics of the nuclear vicinity is greatly influenced by the exact location of the hidden nucleus.

Several authors have addressed this problem, but most of the nuclear positions determined are indirect ones in the sense that they are from lower resolution images than the *HST* images or VLBI maps, and these positions are slightly different from one another (see, e.g., Thatte et al. 1997, and references therein). The only exception so far for pinpointing the location directly on the *HST* high-resolution images is to use imaging polarimetry data. The nucleus can be determined as the center of the centrosymmetric distribution of the position angle (P.A.) of polarization, which is expected to be observed if the radiation from the nucleus is being scattered by the surrounding gas. (We refer to this case as a point-source scattering case hereafter.) Capetti et al. (1995a, 1995b) have determined the nuclear location by this method. However, in their P.A. map, clear deviations from the centrosymmetric pattern are seen, and they did not state whether they are real or discuss the observational error in P.A. at each position of the image. If the deviations are real, the nuclear position determined by them would not be very accurate and reliable.

In this paper, we extend their work to discuss these deviations through the extensive estimation of the observational errors and then to redetermine the location of the nucleus more accurately within a convincing error circle. Our result is that the most probable location of the nucleus has moved to the north by $\sim 0\farcs2$, significantly larger than the quoted error of Capetti et al. (1995b).

The second objective of this paper is to derive the three-dimensional structure of the nuclear region. The *HST* images show that this region has a knotty and filamentary structure. If the UV radiation from each knot is dominated by the scattered radiation, the polarization degrees of the clouds provide the scattering angle at each cloud. Hence, we can derive the three-dimensional distribution of these clouds with respect to the nucleus.

We describe the data in § 2 and error estimation in § 3. In § 4 we examine the P.A. distribution, and in § 5 we discuss the location of the nucleus. Then in § 6 we derive the three-dimensional distribution of the scatterers. We discuss these results in § 7, and our conclusions are presented in § 8. In the Appendix, we summarize the method of error estimation. We assume a distance of 14.4 Mpc to NGC 1068 in this paper (Tully 1988), corresponding to a scale of $1'' \simeq 70$ pc.

2. THE ARCHIVAL DATA

2.1. *Reduction Procedure*

The archival *HST* data used are summarized in Table 1. The polarimetry data were obtained on 1995 February 28. These data have been published by Capetti et al. (1995b). The central small portion was in the 10% level nonlinear regime, so a flat-field linearity correction was applied, but we confirmed that this correction has no significant effect on our analysis by implementing the same analysis below on the data without a linearity correction. The data were subsequently processed in the standard manner to correct for geometric distortion and flat-field response. The reseau marks were removed using neighboring pixels. The back-

[1] Based on observations made with the NASA/ESA *Hubble Space Telescope*, obtained from the data Archive at the Space Telescope Science Institute, which is operated by the Association of Universities for Research in Astronomy, Inc., under NASA contract NAS 5-26555.

TABLE 1

HST/FOC ARCHIVAL DATA USED

Root Name	Filter 1	Filter 2	Exposure time (s)	Date of Observation	Description
x274020at	F253M	POL0	1796.625	1995 Feb 28	UV continuum
x274020bt	F253M	POL0	341.625	1995 Feb 28	
x274020ct	F253M	POL0	1451.625	1995 Feb 28	
x274020dt	F253M	POL60	748.625	1995 Feb 28	
x274020et	F253M	POL60	1044.625	1995 Feb 28	
x274020ft	F253M	POL60	1201.625	1995 Feb 28	
x274020gt	F253M	POL60	591.625	1995 Feb 28	
x274020ht	F253M	POL120	1608.625	1995 Feb 28	
x274020it	F253M	POL120	1796.625	1995 Feb 28	
x24e0102t	F501N	...	1196.000	1994 Jan 10	[O III]
x24e0103t	F501N	F4ND	1196.000	1994 Jan 10	
x24e0106t	F253M	...	1196.000	1994 Jan 10	UV continuum

ground subtraction was implemented using the outermost regions of the images.

These data were obtained after the COSTAR deployment, but at the time of this polarimetry observation *HST* had an extraordinarily poor focus due to a large movement of the secondary mirror, the effect of which will be discussed in detail below. Therefore, the images through different polarizers (POL0, POL60, POL120), which are known to be slightly shifted relative to one another, were registered by using the image shift values of calibrations by Hodge (1993, 1995), not by using pointlike sources in the outer region. Then the images were scaled according to the exposure times and the transmittances of the polarizers and the F253M filter. (The filter transmits the UV radiation around 2400–2700 Å.) Finally these images were combined to obtain the Stokes parameter I, Q, U images.

Using several archival *HST*/FOS spectra taken with 0″.3 aperture, we have estimated the amount of the emission-line contamination in the F253M image to be around the 10%–15% level. This includes, however, the broad Fe II lines that are also a part of the scattered light in addition to the scattered continuum (Antonucci, Hurt, & Miller 1994). Therefore, the effect of the line contamination on the polarization should be much smaller.

We have also used the archival images of NGC 1068 taken through the F501N filter, i.e., the [O III] image, and through the F253M filter but without polarizers, the focus of which seems to be fine. They were obtained on 1994 January 10, also after the COSTAR deployment. They have been published by Macchetto et al. (1994). The images were processed through the same procedure as above, but in the F501N image, the central nonlinear and saturated portion was filled with the appropriately scaled image taken with the F4ND filter. The pattern noise associated with the FOC nonlinearity was removed by Fourier filtering. The registration of these two images was carried out using pointlike sources in the outer region, with uncertainty of less than 1.4 pixel. The registration of this F253M image and the I (total intensity) image from the polarimetry data was done by taking a cross correlation because of the bad focus in the I image. We also tried this registration using point sources and found that the results coincide within 1 pixel.

Both of the observations were implemented in normal 512 × 512 mode, where the pixel size is 0″.014 × 0″.014 and the field of view is 7″ × 7″.

2.2. *HST Focus and Degradation of the Image*

Because of the bad focus in the imaging polarimetry observation, the images have a significant blurring. The effect on the polarization analysis should be significant especially at the region where the gradient of the polarized-flux distribution is large. We first estimate the extent of this blurring by using the fine-focus (nonpolarimetric) F253M image.

To avoid confusion, we call this F253M image without polarizers a sharp UV image and the I image of the polarimetry simply an I image. Synthetic aperture photometry was carried out to take the ratio of the I image to the sharp UV image at various aperture diameters, and the results on a few tens of local maxima over the image were averaged. The results are shown in Figure 1. The scatter of the ratio for each aperture is shown as a vertical line. The expected amount of the error in the ratio due to statistical noise is also shown with horizontal ticks. As we expect that the local peak intensity is lowered by the blurring, the average ratio is certainly less than unity and it becomes smaller with smaller aperture and about 0.9 at 0″.15 aperture, down to ~0.85 at 0″.05 (although the statistical significance of these

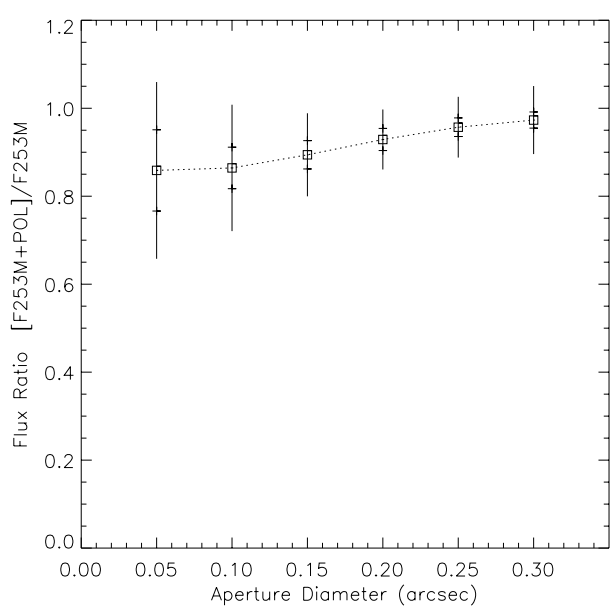

FIG. 1.—Averaged ratio of the I image to the sharp UV image over various aperture diameters is shown as squares, connected by dotted lines. The vertical line on each square represents the standard deviation of the scatter from each averaged ratio. The expected amount of the error in the ratio due to statistical noise is shown in horizontal ticks.

average ratios becomes lower with smaller aperture). The regions in the I image with this ratio larger than ~ 1.0 have significant leaks from the neighboring bright regions.

To infer correctly the degradation of the point-spread function (PSF) of this observation, we have estimated the amount of the secondary mirror motion in the following way. We constructed model PSFs using TinyTim (Krist 1993) with a range of secondary mirror movement and convolved the sharp UV image with those PSFs. Then we compared them to the I image, which is convolved with the PSF of nominal focus for equivalence. We calculated the ratio of these two by the same synthetic aperture photometry as in Figure 1. It is expected that this ratio becomes unity for all aperture sizes when the appropriate amount of the secondary mirror shift is taken for the model PSF. We found that this was the case for a shift of about 9–10 microns. The model PSF at this focus indicates that the FWHM of the PSF was 0".10–0".15 at the time of the observation.

Therefore, we decided to implement our analysis in three ways: (A) 10×10 pixel binning, corresponding to $\sim$0".15 $\times$ 0".15, (B) 20×20 pixel binning, (C) 0".15 aperture diameter synthetic photometry. The size for cases A and C could be too small, but the effect of small aperture will be taken into account in the error estimation. For case C, the aperture centers are selected as the local peaks in the I image, which are thought to represent the positions of the resolved clouds in this nuclear region.

3. ERROR ESTIMATION

In order to examine the P.A. distribution accurately, we need extensive estimation of the observational error in the *HST*/FOC polarimetry. We describe major ideas here and summarize other details in the Appendix.

We estimate the error in polarization degree and P.A. by considering the following four sources of errors that are expected to be major among various error sources.

1. *Statistical error.*—Poisson noise is assumed.
2. *Uncertainty from the image registrations of three polarizer images.*—As described in § 2.1, we have registered the images using the calibrated values of Hodge (1995) and their wavelength dependence by Hodge (1993). The calibrated image shifts have an uncertainty of about ± 0.3 pixel. Therefore we shifted POL60 and POL120 images by this amount along the image x and y axes relative to POL0 image and calculated the resulting change of the polarization.
3. *Polarizer axes uncertainty.*—The transmission axes of each polarizer have nominal values of 180°, 60°, 120° with respect to the $+x$ axis of the image, and those values have about $\pm 3°$ uncertainties (Nota et al. 1996). The errors in the calculated polarization due to this uncertainty were estimated by considering the dependence of the calculated polarization on the polarizer axes' angles (see Appendix for more detail).
4. We consider the uncertainties from the following error sources as the uncertainties in the correction factors to be multiplied to each image through each polarizer.

a) Each polarizer, especially POL60, has a different wavelength dependence of transmittance, so when the spectrum of the object changes from place to place, each polarizer's image has to be multiplied by a different factor to correct for the different effective throughput. By assuming a power-law source spectrum and varying the power-law index in a reasonable range, we estimate that this has effects of less than about 1% in the correction factors.

b) Differences in PSFs through each polarizer result in uncertainties in these multiplying factors locally. We estimate this effect from the result given by Hodge (1995), who has investigated the differences in the fluxes of unpolarized point sources through different polarizers over various aperture sizes. Although this is for data with nominal focus, the maximum uncertainties for our out-of-focus data can be estimated for each of our binning sizes A, B, and C above, from the flux differences of smaller aperture size in the result of Hodge (1995). For cases A and C, the relative discrepancies between the fluxes through each polarizer are expected to be less than 3% to 4%, reading from the plots of Hodge (1995) for 3 to 5 pixel aperture radius, and for case B less than 2% to 3%, from the same plots for $\sim$7 to 10 pixel aperture radius. The fact that the result of Hodge (1995) is for point sources while our sources are more extended gives us additional support that the values above can be considered as the maximum uncertainties.

c) Flat-fielding uncertainty. The flat fields used by the FOC standard calibration are heavily smoothed and they do not correct for the fine-scale features in the original, unsmoothed flat fields. We have estimated the resulting flat-fielding uncertainties by calculating the deviations of the unsmoothed flat field from the smoothed one for the used portion of the image. The results are about 3% for cases A and C, 2% for case B.

Taking the sum of the squares of these *a*–*c* factors, we consider uncertainties in each multiplying factor as 5% for cases A and C, 4% for case B, at most. The effects of these uncertainties on the polarization were calculated from the dependence of the polarization on these multiplying factors (see Appendix for more detail).

The total error was estimated by combining in quadrature all the uncertainties above from 1 to 4. Source 4 is usually larger than 2 and 3. Typically, the total estimated error in the polarization degree σ_P in the regions of sufficient statistical signal-to-noise ratio (S/N) (the portion of the data used in the analysis below) was about 4.5%–5.5% for cases A and C and about 3.5%–4.5% for case B. If the statistical error is excluded, the quadratic sum of the other three was about 4.5% for cases A and C and about 3.5% for case B.

4. EXAMINATION OF POSITION ANGLE DISTRIBUTION

As shown in Capetti et al. (1995b), the overall P.A. distribution is quite centrosymmetric, quite close to a point-source scattering case. However, clear deviations from the centrosymmetric pattern are seen in some regions, especially around the very center (see their Fig. 2). We now examine these deviations and discuss whether the data are really consistent with this simple model, based on the P.A. errors estimated in the previous section and on the investigation of the bad-focus effect discussed in § 2.2.

4.1. *Construction of χ^2 Image*

We evaluate whether the data are really consistent with point-source scattering by calculating the χ^2 value. For each ith binned pixel or aperture, we denote the P.A. data as $\theta_{\rm PA}(i)$, and the ideal centrosymmetric P.A. with a certain symmetric center (x_c, y_c) as $\theta_{\rm ideal}(i; x_c, y_c)$. We write the χ^2

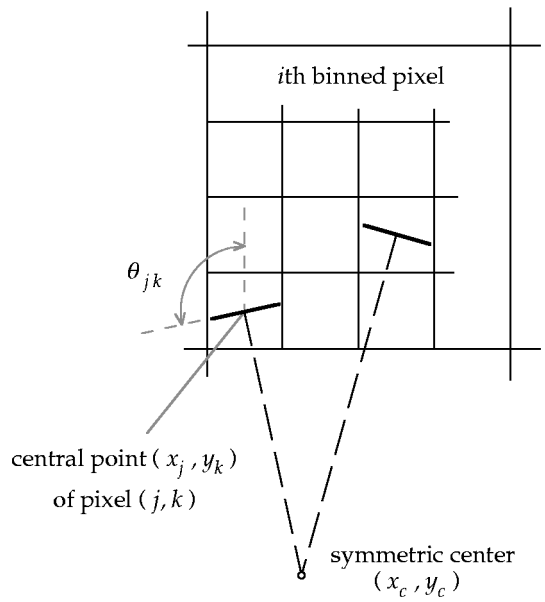

FIG. 2.—Illustrates how the centrosymmetric P.A. for each binned pixel is calculated using the polarized-flux distribution within the binned pixel as weight. Thick solid vectors represent the P.A.s perpendicular to the direction to the symmetric center.

value for (x_c, y_c) as

$$\chi^2(x_c, y_c) = \sum_i^{\text{valid data}} \frac{[\theta_{\rm PA}(i) - \theta_{\rm ideal}(i;\, x_c, y_c)]^2}{\sigma_{\theta_{\rm PA}}(i)^2}\,, \qquad (1)$$

using the total estimated error in P.A. $\sigma_{\theta_{\rm PA}}$ described in the previous section. The χ^2 values for various symmetric centers are calculated, and a χ^2 image is constructed in which the image value at a certain point represents the χ^2 value with this point being the symmetric center.

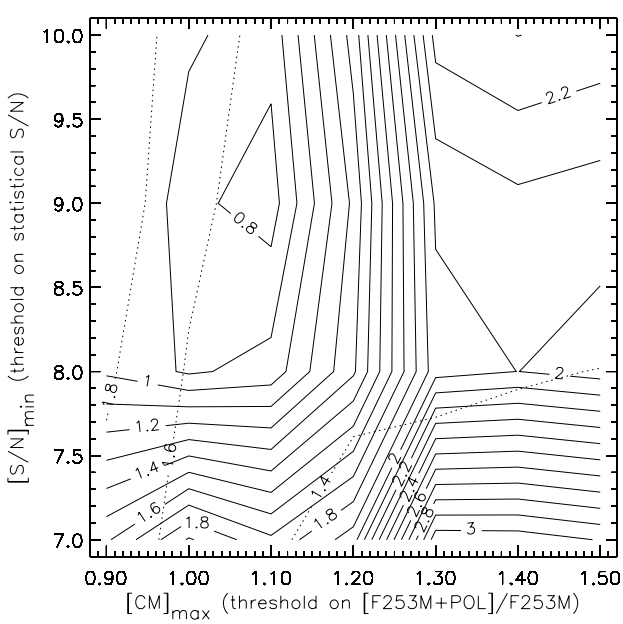

FIG. 3.—Map of the minimum reduced χ^2 for case A is drawn in solid contours on the plane of the thresholds on the contamination measure (ratio of the I image to the sharp UV image) and statistical S/N (P/σ_P). Also shown in dotted contours are the cutoff values of the reduced χ^2 with 99% confidence level for each degree of freedom in each set of thresholds.

The ideal centrosymmetric P.A. for one large binned pixel or aperture depends on, in addition to the direction to the symmetric center, the polarized-flux distribution within that pixel. Therefore we used the original, not binned, distribution of polarized flux within the binned pixel or aperture for the calculation of the χ^2 value. That is, we calculate the polarized-flux–weighted ideal centrosymmetric P.A. (actually, weighted further by the reciprocal of statistical error of polarized flux, to avoid having too much weight on the pixels with low S/N polarized flux) as

$$\theta_{\rm ideal}(i;\, x_c, y_c) = \frac{1}{2}\arctan\frac{U_{\rm ideal}(i)}{Q_{\rm ideal}(i)}\,, \qquad (2)$$

where

$$Q_{\rm ideal}(i) = \frac{\sum_{j,k}^{i\text{th bin}} w_{jk} I_P(j,\, k)\cos 2\theta_{jk}}{\sum_{j,k}^{i\text{th bin}} w_{jk}}\,, \qquad (3)$$

$$U_{\rm ideal}(i) = \frac{\sum_{j,k}^{i\text{th bin}} w_{jk} I_P(j,\, k)\sin 2\theta_{jk}}{\sum_{j,\,k}^{i\text{th bin}} w_{jk}}\,, \qquad (4)$$

$$w_{jk} = \frac{1}{\sigma_{I_P}^{\rm stat}(j,\, k)}\,, \qquad (5)$$

$$\theta_{jk} = \arctan\frac{y_k - y_c}{x_j - x_c}\,. \qquad (6)$$

The quantities $I_P(j, k)$, $\sigma_{I_P}^{\rm stat}(j, k)$, (x_j, y_k) are the polarized flux, statistical error in the polarized flux, and central point for the original pixel (j, k) within the ith binned pixel, respectively. These are illustrated in Figure 2. The summations are taken over all pixels (j, k) within the ith binned pixel. The angle θ_{jk} corresponds to the ideal centrosymmetric P.A. for the center of the pixel (j, k).

This correction in the ideal P.A. (the difference between the polarized-flux–weighted ideal P.A. and the centrosymmetric P.A., which is calculated simply for the center of the binned pixel or aperture) was found to be very important in the central bright and knotty region. In this region, the amount of the correction was larger than the total error of P.A. estimated in § 3.

4.2. *The Effect of Bad Focus on the Evaluation of* χ^2

The extraordinarily degraded PSF of these polarimetry data can affect the P.A. distribution significantly, especially in the pixels surrounding the bright clouds, even with relatively large pixel binning. We eliminate this effect from the analysis by masking out the binned pixels or apertures that are suspected to have a significant leak from the surrounding pixels. If we take the ratio of the I image to the sharp UV image for each bin or aperture, the pixels or apertures that are not affected by the surrounding regions should have this ratio less than around unity, which can also be down to ~ 0.9 for 0″.15 aperture as shown in Figure 1 and discussed in § 2.2. We call this ratio here a contamination measure. We should mask out the region where this contamination measure is much larger than unity, so we set an appropriate threshold on this contamination measure, which we denote as $[\rm CM]_{max}$. In addition, we use only the region where the polarization has been detected with high statistical S/N. We set an appropriate threshold on $P/\sigma_P^{\rm stat}$ (statistical S/N of P), which we write as $[\rm S/N]_{min}$.

The result is that, choosing appropriate thresholds on these two factors, we have obtained minimum reduced χ^2

(the χ^2 divided by degrees of freedom) of slightly less than unity for all three binning cases from A to C. This indeed means that these polarimetry data are totally consistent with point-source scattering, within the accuracy of the FOC polarimetry. In Figure 3, we show the map of the minimum reduced χ^2 value in case A for various sets of $[\mathrm{CM}]_{\mathrm{max}}$ and $[\mathrm{S/N}]_{\mathrm{min}}$. The χ^2 becomes smaller for larger $[\mathrm{S/N}]_{\mathrm{min}}$ and smaller $[\mathrm{CM}]_{\mathrm{max}}$, and we clearly see the χ^2 becomes minimum and almost constant for $[\mathrm{S/N}]_{\mathrm{min}} \geq 8$ and $[\mathrm{CM}]_{\mathrm{max}} \leq 1.1$, with its value indicating the fit is very good. The dotted-line contours indicate the cutoff value of the reduced χ^2 with 99% confidence level for each degree of freedom in each set of $[\mathrm{S/N}]_{\mathrm{min}}$ and $[\mathrm{CM}]_{\mathrm{max}}$. The χ^2 also becomes stable for $[\mathrm{S/N}]_{\mathrm{min}} \geq 8$ and $[\mathrm{CM}]_{\mathrm{max}} \geq 1.3$, but the reduced χ^2 value for this region is rather hard to accept, since it is much larger than the cutoff value. Furthermore, there is a clear transition between these two regions where the gradient of χ^2 is large and χ^2 switches to an acceptable value when $[\mathrm{CM}]_{\mathrm{max}}$ becomes smaller. Similar results have been obtained for cases B and C. Therefore we conclude that the P.A. distribution is consistent with a point-source scattering only when the contaminated regions are excluded.

5. THE LOCATION OF THE NUCLEUS

Now that the point-source scattering fit is proved to be acceptable, we can discuss the most probable location of the nucleus as the position of the minimum χ^2 point and its error as the contour of the χ^2 image.

5.1. *Minimum χ^2 Point*

We show the P.A. distribution and the point with the χ^2 being minimum for each case A, B, and C in Figures 4, 5, and 6, respectively. The observed P.A.s for each binned pixel or aperture are shown in two white vectors that correspond to $\theta_{\mathrm{PA}} \pm \sigma_{\theta_{\mathrm{PA}}}$, where $\sigma_{\theta_{\mathrm{PA}}}$ is the total estimated error in P.A. Also shown in black vectors are the polarized-flux–weighted ideal centrosymmetric P.A. with the symmetric center being the minimum χ^2 point, marked as a plus, for each binning case. For these figures, we have chosen $[\mathrm{CM}]_{\mathrm{max}}$ to be 1 in all cases, which is considered to be a natural constraint on the contamination measure (although

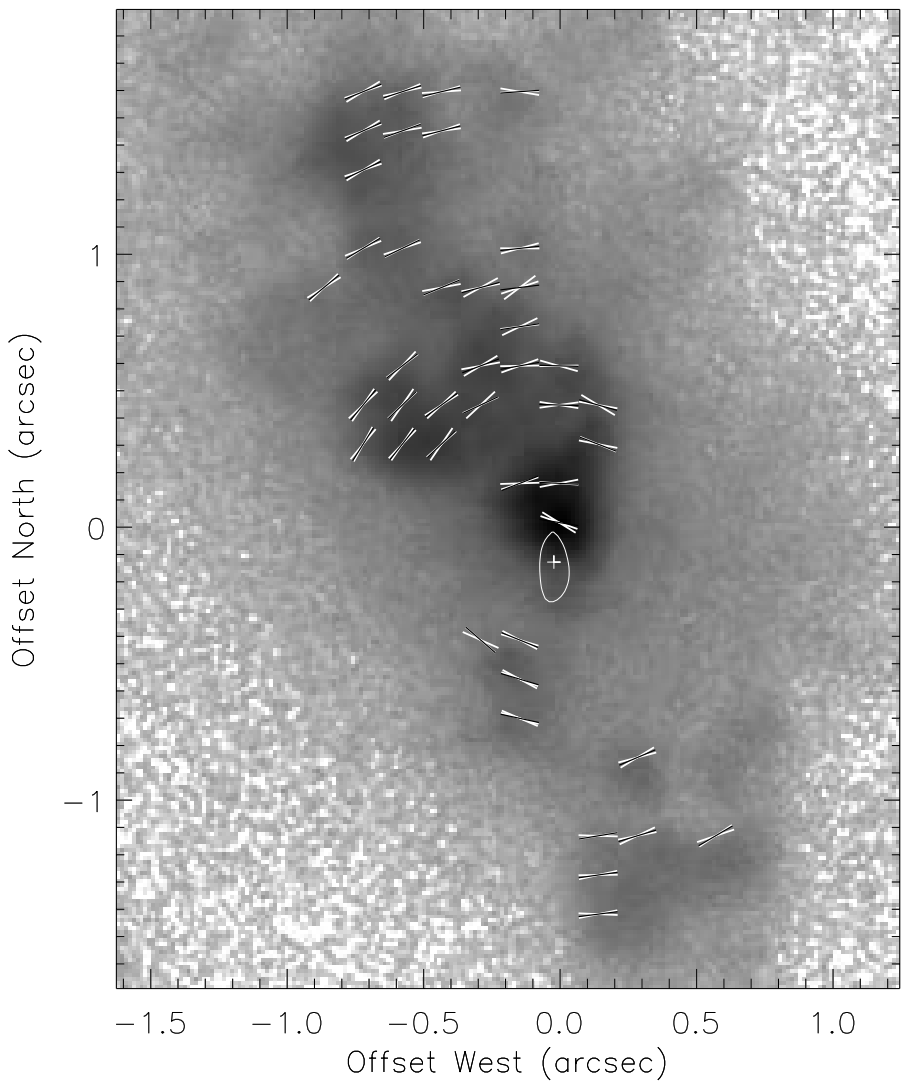

FIG. 4.—P.A. distribution with 10 × 10 pixel binning (case A) is shown on the *I* image of the UV polarimetry. The position of minimum χ^2 is shown as a plus sign, and the error circle of 99% confidence level is also drawn. The two white vectors for each binned pixel indicate $\theta_{\mathrm{PA}} \pm \sigma_{\theta_{\mathrm{PA}}}$, and the black vector shows polarized-flux–weighted ideal centrosymmetric P.A. with the minimum χ^2 position being the symmetric center. The image is in log scale and has been cut at 0.01% of the peak intensity.

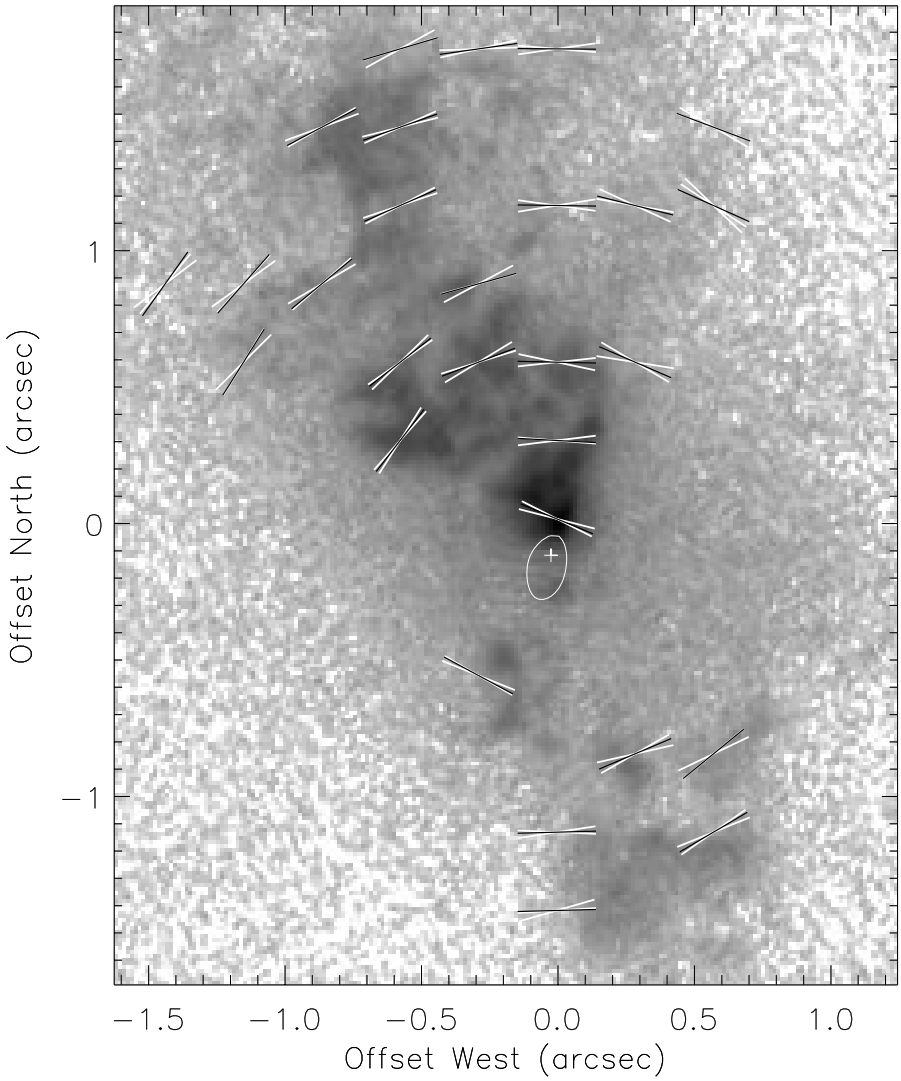

FIG. 5.—Same as Fig. 4, but with 20 pixel binning (case B), and the underlying image is the sharp UV image,which was taken when the *HST* focus was fine. The image is in log scale and has been cut at 0.01% of the peak intensity.

we can also take the values of up to ~ 1.1 to allow for the statistical noise, as seen in Fig. 3). We have taken the lowest $[S/N]_{min}$ in each binning case that could yield acceptable χ^2 values, in order to include as large an area as possible. The minimum reduced χ^2 value was found to be 0.88 for 41 degrees of freedom with $[S/N]_{min} = 8$ in case A, 0.80 for 26 degrees with $[S/N]_{min} = 7$ in case B, and 0.74 for 28 degrees in case C. The underlying image in Figures 4 and 6 is the *I* image, while the sharp UV image is presented in Figure 5 for comparison.

Compared to the previous result from the same data (Capetti et al. 1995b), the minimum χ^2 point, i.e., the most probable location of the nucleus, is very close to the UV brightest cloud, in all cases from A to C, as seen in Figure 7 covering just the central $\sim 0''.5$ region. The white dash-dotted contour represents the UV image, while underlying is the [O III] image through the F501N filter. Our minimum χ^2 points shown in small plus signs are only about $0''.12$ south from the UV peak at the origin of the coordinates, whereas Capetti et al. (1995b) have located the nucleus at $0''.3$ south from the UV peak (the value is actually taken from Capetti, Macchetto, & Lattanzi 1997), shown as a large plus sign with its size being their estimated error.

The reason for this difference is quite clear. Corresponding to the transition of the minimum χ^2 value in Figure 3 from $[CM]_{max}$ of 1.3 to 1.1, we have found that the position of the minimum χ^2 point experiences the transition from $\sim(0''.01, -0''.23)$, which is almost within the error of the Capetti et al. (1997) point, to our points $\sim(-0''.03, -0''.12)$. We found two regions on the plane of $([CM]_{max}, [S/N]_{min})$ where the position of the minimum χ^2 point is stable, just corresponding to the two regions in Figure 3 where the minimum χ^2 values are almost constant. These results are for case A, but we see quite similar results for cases B and C. Therefore, the difference between the two locations is expected to arise from the masking-out procedure for the regions contaminated by the focus effect.

The reason for the shift of this direction is also fairly clear. We show the P.A. distribution in the masked-out region in Figure 8, enclosed by white lines, in addition to the P.A. distribution already shown in Figure 4. The masked-out region, especially around the UV peak, seems to direct the nucleus to the south. So the minimum χ^2 point moves to the north when these regions are excluded.

These P.A.s in the masked-out regions clearly cannot be fitted by point-source scattering, and we have certainly

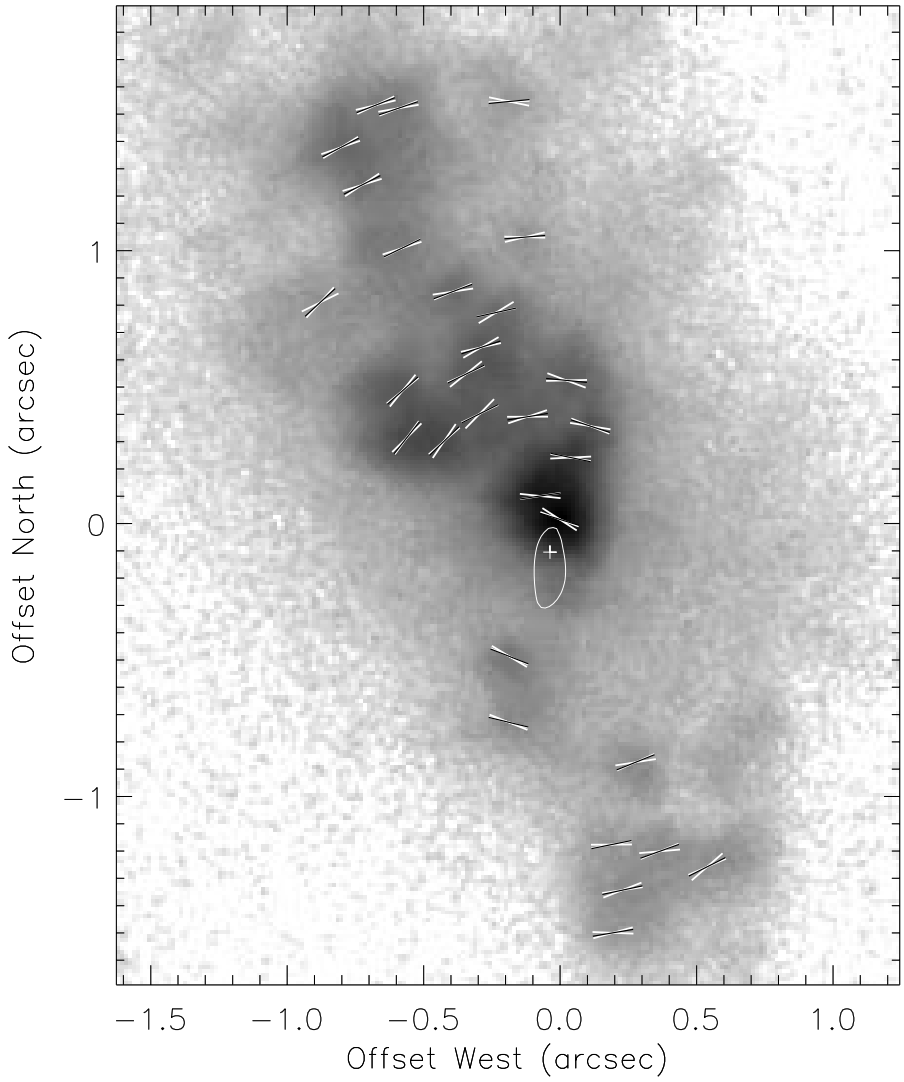

FIG. 6.—Same as Fig. 4, but for the case of aperture photometry on the local peaks with 0″.15 diameter (case C). The underlying image is the *I* image from the imaging polarimetry. It is in log scale and has been cut at 0.1% of the peak intensity to show the bright regions more clearly.

shown that the minimum χ^2 becomes acceptable only if we mask out these regions. The tendency is that the deviations in these regions can be explained by the contamination from the neighboring bright regions. Since our masking-out procedure is quite natural and reasonable, and this tendency gives us further support for our procedure, we conclude that the Capetti et al. (1997) point should be revised to a more northern point, indicated by our minimum χ^2 positions.

5.2. *Error Circle*

The error of the location of the symmetric center can be estimated as contours of the χ^2 image. The contour of 99% confidence level has been drawn for each binning method in Figures 4–6, and these three different contours are all shown with an enlarged scale in Figure 7 in three different white circles. These three are slightly different from one another. This is partly due to the uncertainties in our estimation of P.A. errors, but the error circle for case B is smaller in the north-south direction partly due to the fact that the valid data points in case B are more extended to the east and west (Fig. 5), while in cases A and C they are only extended to the north and south.

As we described in § 3, the uncertainty in the correction factor should be considered as the maximum possible, which might be indicated also by the fact that our minimum χ^2 value is slightly smaller than unity. We have also implemented the calculation of χ^2 with a slightly smaller value for this uncertainty and found that the minimum χ^2 points and northern part of the error circles were almost stable, whereas the southern part of the error circles moved slightly to the north. This shift is about 0″.05 if we take the uncertainty in the correction factor to be 4% for cases A and C and 3% for case B, instead of 5% for A and C and 4% for B. In Figure 7, the error circle of 99% confidence level has been drawn as a black contour for case B with 3% uncertainty in the correction factor. The minimum χ^2 values were 1.16, 1.06, and 0.99 for cases A, B, and C, respectively, which are still low enough to accept the fit. Therefore, the error circle would be smaller in the southern part.

The brightest [O III] cloud in Figure 7 is called cloud B and the fainter cloud 0″.2 to the south is called cloud A (Evans et al. 1991; see also Bland-Hawthorne et al. 1997). Cloud B is slightly but significantly displaced from the brightest UV cloud, where the offset is about 0″.05 at P.A. $\sim -37°$. These are consistent with the values noted by

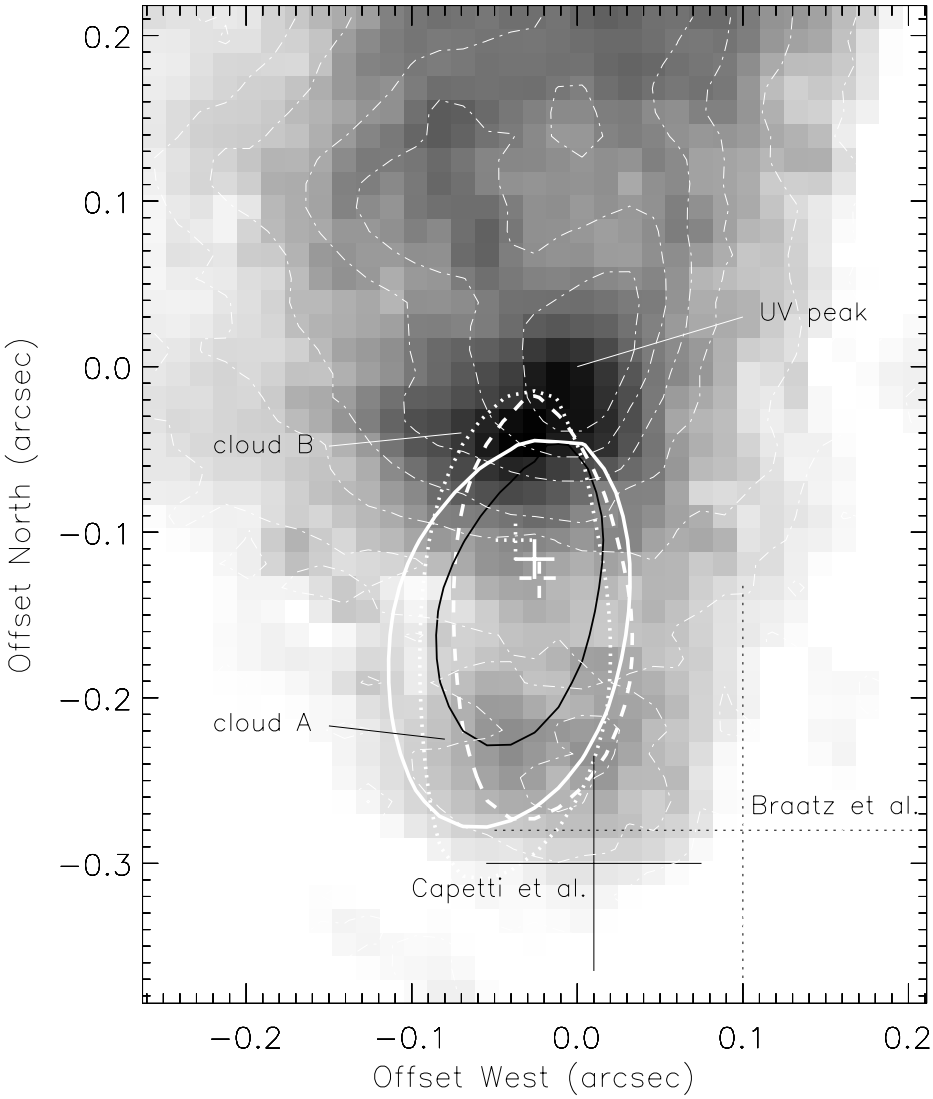

FIG. 7.—Enlarged view of the central ∼0″.5 region. The positions for minimum χ^2 points and 99% confidence level contours are shown in white dashed, solid, and dotted line for cases A, B, and C, respectively. The black solid contour represents 99% confidence level error circle for case B with smaller uncertainty in the correction factor. Underlying is the F501N [O III] image, and the dash-dotted contours represent the sharp UV image. Both are in log scale. The thin solid and dotted plus sign indicates the nucleus location suggested by Capetti et al. (1995b) and Braatz et al. (1993), respectively, with their sizes being the errors estimated by the respective authors.

Macchetto et al. (1994). Note that the accuracy of the registration of these two images is estimated to be better than 1.4 pixel, corresponding to 0″.020, as described in § 2.1. The error circles suggest that the nucleus is located between clouds A and B. The projected distance between cloud B and our minimum χ^2 point is only ∼0″.08 (∼6 pc). Cloud B is only marginally rejected as the symmetric center. This means both that the quality of these FOC polarimetry data can only limit the location with this amount of error, and that the nucleus could be located just beside cloud B.

For comparison, the location of the nucleus determined by Braatz et al. (1993) as the peak position at 12.4 μm has

TABLE 2

POSITIONS OF NUCLEUS AND OTHER SOURCES

Source Name	Offset West (arcsec)[a]	Offset North (arcsec)[a]	R.A. (J2000)	Decl. (J2000)
UV and optical peak.....	0.00	0.00	02 42 40.711 ± 0.005	−00 00 47.81 ± 0.08[b]
Hidden nucleus	−0.03 ± 0.05	$-0.12^{+0.07}_{-0.12}$	02 42 40.713 ± 0.006	$-00\ 00\ 47.93^{-0.11}_{+0.14}$[c]
S1 source	0.02 ± 0.10	−0.13 ± 0.10[b]	02 42 40.710 ± 0.001	−00 00 47.94 ± 0.02[d]

NOTE.—Units of right ascension are hours, minutes, and seconds, and units of declination are degrees, arcminutes, and arcseconds.

[a] Offset from UV and optical peak.

[b] From Capetti et al. 1997.

[c] Quadratic sums were taken to obtain errors.

[d] From Muxlow et al. 1996.

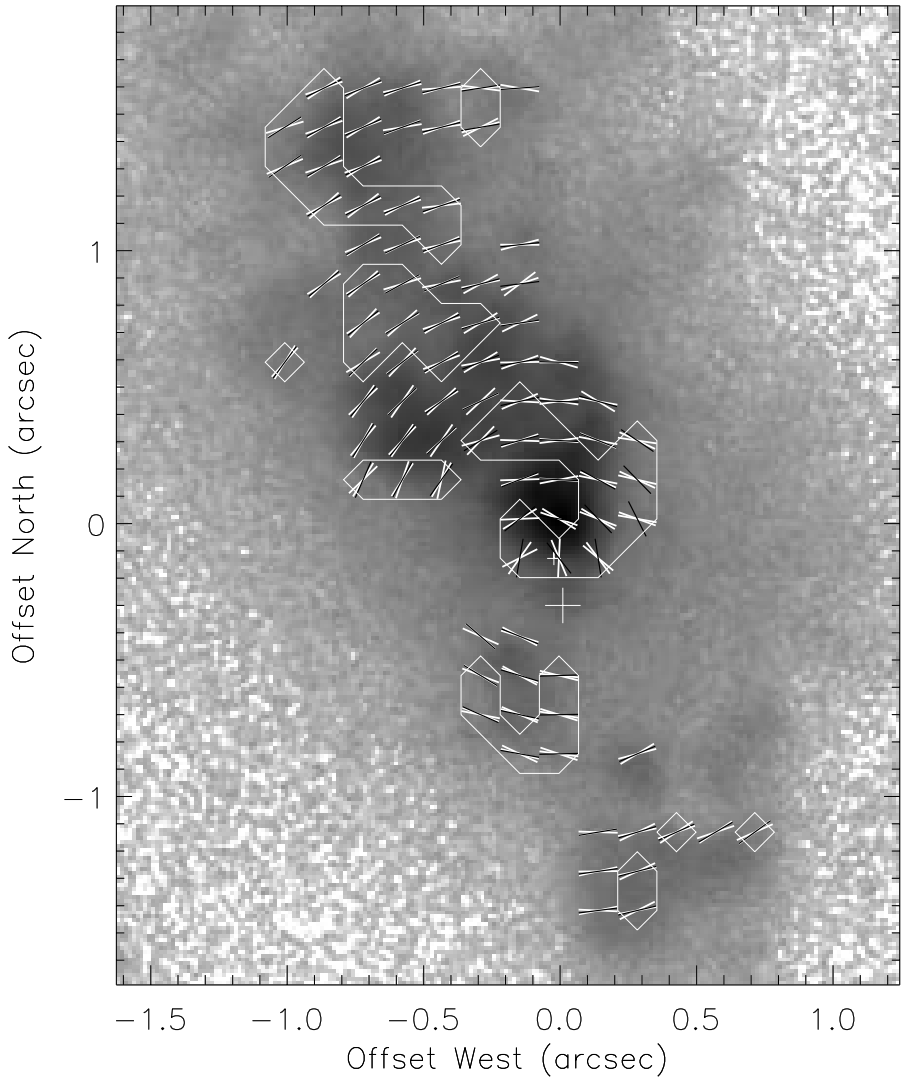

FIG. 8.—Same as Fig. 4 but the observed P.A.s in the masked-out region, enclosed by white lines, are also drawn. The small plus sign is the same as in Fig. 4, while the large plus sign represents the location of the nucleus suggested by Capetti et al. (1995b), with its size being their estimated error.

been drawn in Figure 7, with the size being their estimated error. This location is given with respect to the optical continuum peak, but we have used their value with respect to the UV peak instead, since the UV peak and optical peak are coincident within the accuracy of the registration of *HST*/WFPC2 and FOC images (Capetti et al. 1997; Kishimoto 1999). Our minimum χ^2 positions are marginally within their error box. Thatte et al. (1997) have also located the nucleus as the peak of near-infrared emission, which is slightly north of, but almost identical to the position of Braatz et al. (1993).

In conclusion, allowing for the displacement of the minimum χ^2 points and error circles of the four cases in Figure 7, we locate the nucleus 0".12 south and 0".03 east from the UV peak, with the error circle extending from this point about 0".07 to the north, 0".12 to the south, and 0".05 to the east and west. In Table 2, we summarize this result with equatorial coordinates, using the result of absolute astrometry by Capetti et al. (1997) on the *HST* continuum peak.

6. THREE-DIMENSIONAL STRUCTURE

We have shown that the UV polarization is really consistent with point-source scattering and determined the location of the nucleus accurately. Based on these two results, we infer the three-dimensional structure of the nuclear region by using the polarization degrees as the indicator of scattering angles or viewing angles at each resolved cloud in the image.

6.1. *Assumptions*

Interpretation of the polarization degree is usually difficult because of the existence of unpolarized, diluting radiation in terms of polarization, such as starlight. In the nuclear region of NGC 1068, however, there is some evidence that suggests the diluting radiation in the UV range is fairly small, as described below. If this is correct, we are in the unusual situation that we can infer the distribution of the nuclear resolved clouds three-dimensionally. The polarization degree reflects the angle between our line of sight to the scatterers and the line of sight of those scatterers themselves to the illuminating source, which we call here viewing angles of the scattering clouds, as shown in Figure 9*a*. If we obtain the viewing angles of each cloud, we can locate each cloud along the line of sight with respect to the central radiation source, and thus we will be able to have a three-dimensional view of this nuclear region.

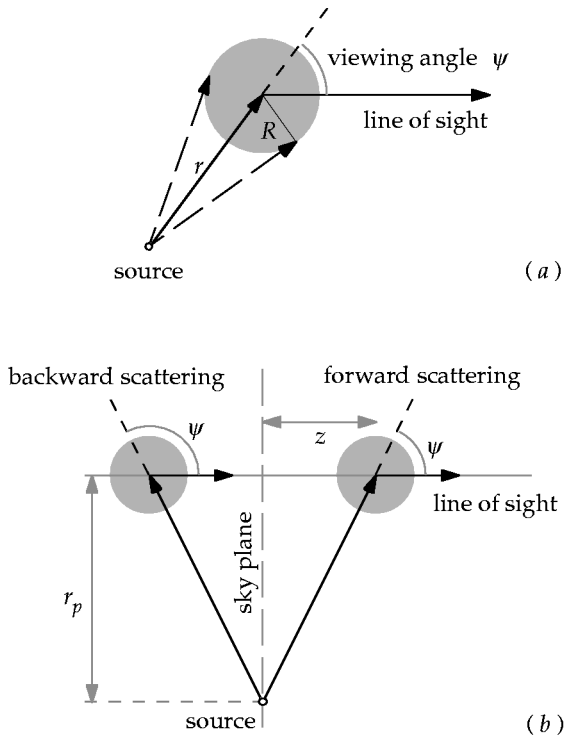

FIG. 9.—Illustrates the configuration of the cloud model. (*a*) Definition of viewing angle of a spherical cloud. (*b*) The two critical positions determined from the polarization of the cloud.

We simply assume here that the UV radiation consists of only radiation scattered by free electrons and no other diluting component exists. This is based on the following two observational arguments in NGC 1068.

1. *HST*/FOS UV spectropolarimetry shows that the polarization is almost constant over the UV range, and its degree declines only in the wavelength longer than ~2800 Å (Antonucci et al. 1994). This has been interpreted to mean that the starlight contribution is significant only in the redward of 2800 Å, almost outside the F253M filter transmission.

2. The same FOS spectropolarimetry, as well as the ground-based spectropolarimetry, shows no evidence of any enhancement in polarization in the broad lines relative to the nuclear continuum. The broad lines are believed to originate only in a region much more compact than the scattering region that we have seen in our imaging polarimetry data. Any diluting radiation such as starlight or free-free emission from the scattering region itself (Tran 1995c), only dilutes the polarization of the scattered continuum, not the scattered broad lines. Therefore, if diluting radiation were present, the polarization would be higher in the broad lines than in the continuum, which has been observed in several Seyfert 2 galaxies, but not in NGC 1068 (Antonucci et al. 1994; Tran 1995a, 1995b).

Those spectropolarimetric data, however, cover a large area, 4″.3 × 1″.4 aperture in the data of Antonucci et al. (1994) and a 2″.4 wide slit in the data of Tran (1995a, 1995b), which could mean that the assumption of scattered-light domination might be true only in the brightest clouds. Therefore we restrict ourselves to use only the polarization degree of the bright knots. We will discuss the validity of this assumption again in § 7.2.

The following method for obtaining the three-dimensional gas distribution and its result have been discussed in Kishimoto (1997). We present the method and results here, with the errors in the observed polarization that have been estimated in much more detail, and with the position of the nucleus that has been obtained more accurately.

6.2. *Method*

The polarization of the scattered radiation from a cloud depends basically on its viewing angle, but also on the size of the cloud compared to the distance to the illuminating source. This effect is large if the cloud is very close to the source. In this section, we describe a simple method for interpreting the degree of polarization, taking this effect into account.

Consider a spherical, uniform cloud of radius R, which is optically thin to scattering. The cloud is illuminated by a point source from a distance r (see Fig. 9*a*). We consider only electron scattering because the primary scatterers in the innermost region of NGC 1068 are thought to be electrons (Antonucci & Miller 1985; Miller, Goodrich, & Matthews 1991). The calculation of polarization for optically thin systems of axisymmetric distribution has been implemented by Brown & McLean (1977). We follow their naming conventions for a geometrical factor α and shape factor γ. Our three quantities, polarization of the scattered radiation P, viewing angle ψ, and the relative cloud radius $\eta \equiv R/r$, are related as

$$P = \frac{-\sin^2 \psi}{2\alpha(\eta) + \sin^2 \psi}, \tag{7}$$

where $\alpha(\eta)$ is a function of η and defined as

$$\alpha \equiv (1 + \gamma)/(1 - 3\gamma). \tag{8}$$

We find the shape factor γ as

$$\gamma = \frac{\eta^3}{2k(\eta)} + \frac{1 - \eta^2}{4}, \tag{9}$$

where

$$k(\eta) = \eta - (1 - \eta^2) \ln \frac{1 + \eta}{\sqrt{1 - \eta^2}}. \tag{10}$$

Since the projected distance $r_p \equiv r \sin \psi$ is the observational quantity whereas the actual distance r is not, we rewrite η as

$$\eta = \eta' \sin \psi, \quad \text{where } \eta' \equiv R/r_p. \tag{11}$$

These relations are rather complicated, but for small η, γ becomes close to unity, hence α close to -1, and equation (7) becomes the well-known equation for Thomson scattering as

$$P = \frac{1 - \cos^2 \psi}{1 + \cos^2 \psi}. \tag{12}$$

This means that the shape of the cloud or the distribution of the gas inside the cloud does not affect the polarization of the scattered radiation if the cloud size is small enough compared with the distance to the illuminating source, and the polarization depends only on the viewing angle, as a natural consequence.

The three-dimensional positions of the clouds can now be obtained, given the position of the central source in the

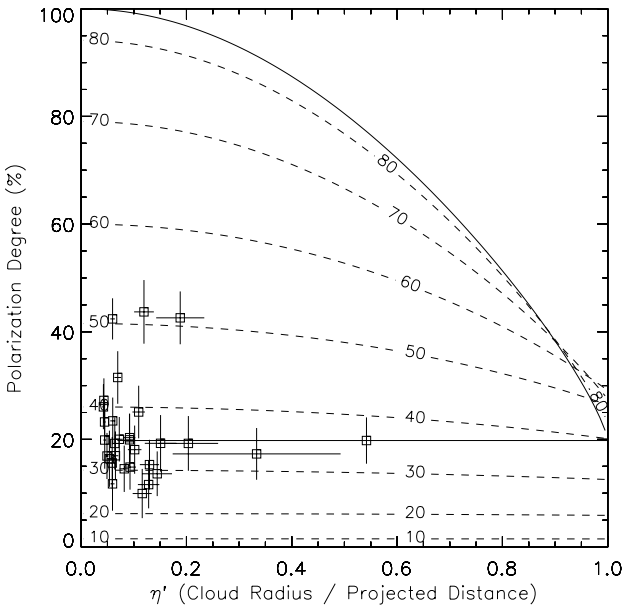

FIG. 10.—Map of viewing angle ψ on the plane of (η', P). The observed positions of each cloud are also shown as squares with errors.

image (x_c, y_c). If we denote the position of the center of each cloud in the image as (x, y), the distance z for each cloud from the sky plane in which the nucleus resides (see Fig. 9*b*) is written as

$$z = r_p/\tan\psi \ , \tag{13}$$

where

$$r_p = \sqrt{(x - x_c)^2 + (y - y_c)^2} \ . \tag{14}$$

One of the ambiguities in this method is that because of the forward-backward symmetry of the optically thin electron scattering, there are two possible viewing angles derived from a single value of polarization, i.e., the forward and backward scattering case. These two angles correspond to the two positions along the line of sight, shown as Figure 9*b*. Also, if a cloud is not sufficiently resolved, several clumps may exist along one line of sight. This could be the limit of our method, but in this case, the two positions derived from the polarization set a constraint on the positions of the clouds. If there is a scattering clump between these two positions, there must be another one outside of these two positions, to dilute the highly polarized scattered light from the inner clump. In this sense, these two positions

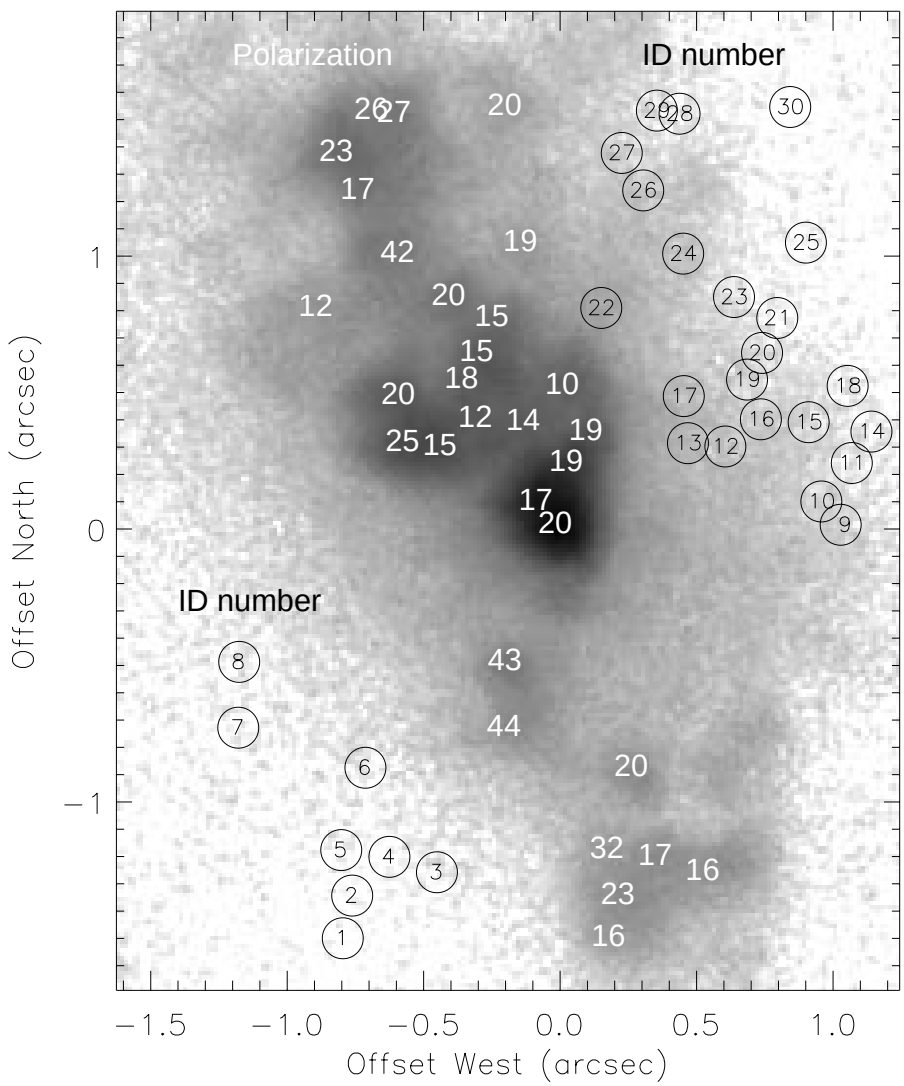

FIG. 11.—Observed polarization degree of each cloud is shown on the center of each cloud in white numbers. The ID numbers for each cloud are also shown as black numbers in circles, displaced to the east and west for lower and upper positions, respectively.

TABLE 3

POLARIZATION AND THREE-DIMENSIONAL POSITION OF CLOUD

ID Number	x (arcsec)	y (arcsec)[a]	R.A. (J2000) (02^h04^m+)	Decl. (J2000) ($-00°00'+$)	P (percent)	θ_{PA} (deg)	ψ (deg)	z (arcsec)
1	0.19	−1.50	40.698	49.31	16.4 ± 5.2	96.6 ± 8.9	32.1 ± 4.9	2.23 ± 0.42
2	0.23	−1.34	40.696	49.15	23.4 ± 4.3	104.9 ± 6.6	38.1 ± 3.4	1.60 ± 0.19
3	0.54	−1.26	40.675	49.07	15.6 ± 4.8	122.3 ± 9.0	31.3 ± 4.7	2.09 ± 0.38
4	0.36	−1.20	40.687	49.01	17.0 ± 4.5	103.5 ± 8.5	32.6 ± 4.1	1.80 ± 0.29
5	0.19	−1.18	40.698	48.99	31.5 ± 4.9	95.4 ± 5.1	43.8 ± 3.2	1.12 ± 0.13
6	0.28	−0.87	40.693	48.68	20.3 ± 4.5	106.4 ± 7.4	35.6 ± 3.7	1.14 ± 0.16
7	−0.19	−0.73	40.724	48.54	43.7 ± 5.9	71.5 ± 3.5	51.4 ± 3.4	0.50 ± 0.06
8	−0.19	−0.49	40.723	48.30	42.6 ± 4.9	62.8 ± 3.8	50.9 ± 2.9	0.32 ± 0.03
9	0.00	0.02[b]	40.711	47.79	19.8 ± 4.3	63.2 ± 6.3	36.0 ± 3.9	0.19 ± 0.03
10	−0.07	0.10	40.716	47.71	17.3 ± 4.8	91.2 ± 7.3	33.2 ± 4.5	0.34 ± 0.06
11	0.04	0.24	40.708	47.57	19.3 ± 5.1	86.4 ± 6.4	34.7 ± 4.4	0.53 ± 0.09
12	−0.42	0.30	40.739	47.51	15.3 ± 4.6	138.4 ± 7.5	31.1 ± 4.5	0.96 ± 0.17
13	−0.56	0.31	40.748	47.50	25.1 ± 4.9	139.2 ± 4.9	39.3 ± 3.7	0.84 ± 0.11
14	0.11	0.36	40.704	47.45	19.3 ± 5.3	74.7 ± 6.3	34.7 ± 4.5	0.72 ± 0.12
15	−0.12	0.39	40.719	47.42	13.6 ± 4.2	99.5 ± 9.3	29.3 ± 4.3	0.92 ± 0.16
16	−0.29	0.40	40.731	47.41	11.6 ± 4.4	125.6 ± 10.0	27.2 ± 5.0	1.14 ± 0.25
17	−0.58	0.49	40.749	47.32	19.9 ± 4.8	135.2 ± 6.1	35.2 ± 4.1	1.16 ± 0.18
18	0.02	0.52	40.709	47.29	9.9 ± 4.6	80.3 ± 11.0	25.2 ± 5.6	1.37 ± 0.35
19	−0.35	0.55	40.734	47.26	18.1 ± 4.5	121.7 ± 7.2	33.6 ± 4.0	1.11 ± 0.17
20	−0.29	0.65	40.730	47.16	14.9 ± 4.2	111.4 ± 9.0	30.6 ± 4.2	1.37 ± 0.23
21	−0.23	0.77	40.727	47.04	14.5 ± 4.3	111.9 ± 9.5	30.3 ± 4.3	1.57 ± 0.27
22	−0.88	0.81	40.770	47.00	11.7 ± 5.0	127.0 ± 10.9	27.3 ± 5.6	2.44 ± 0.59
23	−0.39	0.85	40.737	46.96	20.0 ± 4.1	105.7 ± 7.1	35.3 ± 3.5	1.46 ± 0.19
24	−0.58	1.01	40.750	46.80	42.4 ± 3.8	112.1 ± 4.1	50.5 ± 2.2	1.03 ± 0.08
25	−0.13	1.05	40.720	46.76	19.3 ± 4.9	96.0 ± 7.6	34.6 ± 4.2	1.70 ± 0.27
26	−0.73	1.24	40.759	46.57	16.9 ± 4.3	115.4 ± 8.2	32.6 ± 4.0	2.39 ± 0.36
27	−0.80	1.38	40.765	46.43	23.2 ± 4.2	115.2 ± 6.2	37.9 ± 3.2	2.17 ± 0.25
28	−0.59	1.52	40.750	46.29	27.2 ± 4.1	105.5 ± 5.7	40.9 ± 2.9	2.00 ± 0.21
29	−0.68	1.53	40.756	46.28	26.0 ± 4.1	109.4 ± 6.0	40.0 ± 3.0	2.11 ± 0.23
30	−0.19	1.55	40.723	46.26	19.9 ± 5.3	85.1 ± 6.9	35.2 ± 4.5	2.38 ± 0.40

NOTE.—Units of right ascension are seconds, and units of declination are arcseconds.

[a] Measured from the UV peak, which is taken as the peak position in the sharp UV image (with fine focus).

[b] The position of the maximum intensity in the I image (total intensity, out of focus) is slightly different from that in the sharp UV image.

should be considered as the critical positions. Having these ideas in mind, we simply assume that there is only one cloud along one line of sight.

6.3. *Three-dimensional Mapping*

Given the position of the nucleus (x_c, y_c), the viewing angle ψ can be calculated numerically from the two observational quantities, polarization P and the relative size of cloud η', using equations (7)–(11). Figure 10 shows the map of the viewing angle on the plane of (η', P) for a forward scattering case. There is an upper limit in P for certain η' when ψ is 90°. This maximum polarization becomes smaller for larger η'. This is regarded as a geometrical dilution of polarization, where the position angles of polarization of the scattered light from different places inside the cloud become significantly different so that the polarization tends to cancel out. As a consequence, there is a region of uncertainty at around $\eta' = 0.9$–1.0 and $P = 25\%$–35%, where two viewing angles can be solutions for a single point of (η', P). For the observational points in this region, with certain values for the errors in η' and P, we can obtain the viewing angle only with a large uncertainty.

In Figure 10, we have plotted the observational points of the clumps assuming that the cloud radius is our aperture radius 0″.15/2, with the total error in P estimated in § 3, and the error in η' that originates from the error in the position of the nucleus. We have taken the error of the nuclear position symmetrically as (−0″.03 ± 0″.05, −0″.12 ± 0″.10) for simplicity. Except the central few clouds, we see the viewing angles are well approximated by equation (12), which is the relation for $\eta' = 0$. This means that the cloud shape or gas distribution inside the cloud does not affect the result as described above, although we have used equation (7) to derive the viewing angles for all the clumps. The polarization for each cloud is shown in Figure 11. The results are summarized in Table 3, with equatorial coordinates as in Table 2.

The errors in ψ and z are calculated only from the error in P in Table 3, and we did not include the error in the nucleus position, since it has a systematic effect on *all* clouds. The polarization degrees have been debiased following Simmons & Stewart (1985). That is, the final S/N in polarization, P/σ_P, where σ_P is the total uncertainties in P as estimated in § 3, is large enough for all the clumps so that we are allowed to use the equation given in Wardle & Kronberg (1974),

$$P_{\rm corrected} = P_{\rm obs}\sqrt{1 - \left(\frac{\sigma_P}{P_{\rm obs}}\right)^2}\,, \qquad (15)$$

where $P_{\rm obs}$ is calculated simply as $(Q^2 + U^2)^{1/2}/I$.

From these data, we have constructed the three-dimensional view of the nuclear region in Figure 12. Each cloud is illustrated as a sphere with 0″.15 diameter. The

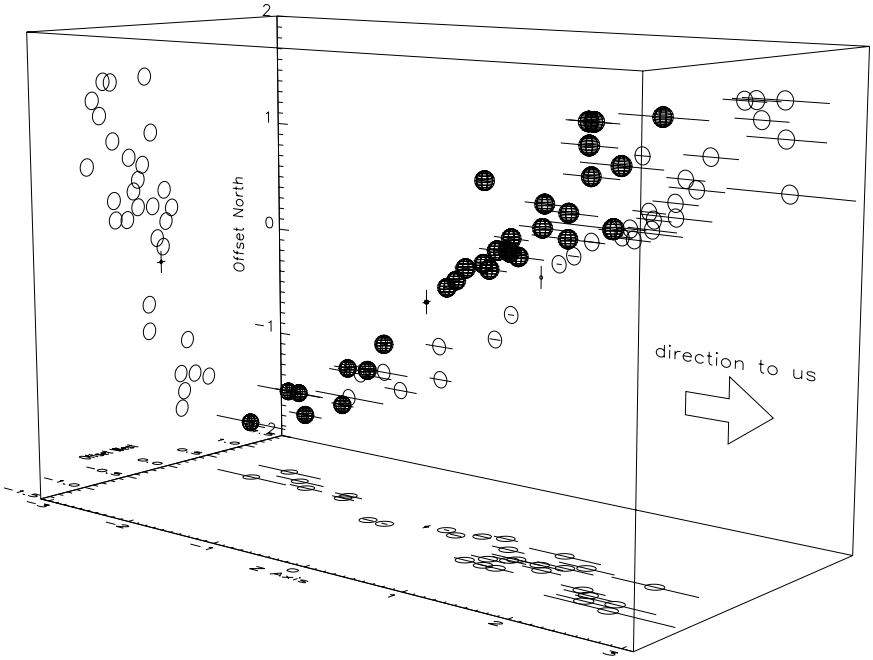

FIG. 12.—Three-dimensional view of the nuclear region. Each cloud is drawn as a sphere of diameter 0″.15, and the nucleus is shown as a smaller sphere in the center, with the errors in its position. The scale unit is 1″. The projected views are also illustrated on each coordinate plane with each cloud drawn as an open circle. The direction to us is indicated by the large white arrow. The error in the position of the cloud center along the line of sight is indicated by the solid line for each cloud.

position of the nucleus is shown as a smaller sphere with its error. The solid line at each cloud indicates the error of its position from the uncertainties in P. The positions in this figure would be only for one of the two possible cases. We could select another side of the critical positions for each cloud, or even both. However, as we also discuss in the next section, there is observational evidence that suggests an absorption excess in the southern region compared to the northern region, from a color difference (Macchetto et al. 1994) and H I absorption (Gallimore et al. 1994). Therefore we have simply selected the case shown in Figure 12.

7. DISCUSSION

7.1. *P.A. Map*

We have shown that the UV polarization image is completely consistent with a point-source scattering within the accuracy of the FOC polarimetry, over wide regions from ~ 100 pc scale down to ~ 10 pc scale around the nucleus. The scattered radiation is very extended to the east and west, as well as to the north and south, as shown in Figure 5. We should note, however, that there could be much smaller deviations from a point-source scattering, which we cannot discuss with the given limit of the accuracy of these imaging polarimetry data. We just certainly do not see any significant deviations from a centrosymmetric pattern beyond the estimated errors of the data when we exclude the regions contaminated by the effect of the bad focus.

Young et al. (1996) have estimated the size of the torus that is thought to be obscuring the nucleus. They have calculated its size to be greater than 200 pc ($\sim 3''$) in diameter, based on the absorption feature at $\sim 1''$ south from the nucleus in their near-infrared polarized-flux image. In Figure 13, we have plotted the UV intensities of each cloud against the projected distance of each cloud from the nucleus, with the error of the projected distance originating from the error in the position of the nucleus. The statistical errors of the UV intensities were quite small, so they are not shown in the figure. We clearly see that the fluxes of the southern clouds (1–8) are systematically smaller than those of the northern clouds, which suggests an absorption excess in the south. However, if we assume that the radial distribution of the UV flux is the same in the south as in the north, the observed UV flux ratio suggests an absorption of only $A_V \lesssim 1$ at $\sim 0''.5$–$1''$ south from the nucleus. The obscuring torus could be extended to this scale, but it should be much smaller if we define it as the absorbing material that has

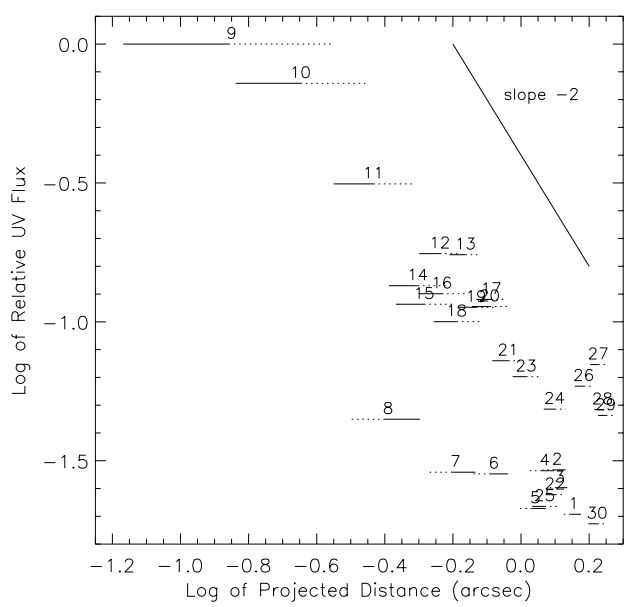

FIG. 13.—Relative UV flux for each cloud in Fig. 11 is plotted as its ID number, against the projected distance from the nucleus, in log scale. The horizontal lines represent the error in the projected distance, where the solid (dotted) ones are for the case with the nucleus shifted to the north (south). The slope of −2 is indicated in the upper right.

enough optical thickness to hide the scattered radiation completely. The size of this material must be less than 0″.3 projected onto the sky, which corresponds to ~20 pc, based on the distribution of the polarization seen in Figure 4.

Muxlow et al. (1996) and Gallimore, Baum, & O'Dea (1996a) argue that the most probable location of the nucleus in the VLBI radio image is one of the most southern components, called the S1 source (Gallimore et al. 1996c). Strong water maser sources have been found at this S1 source (Gallimore et al. 1996b; Greenhill et al. 1996; Greenhill & Gwinn 1997), and these sources have been interpreted to be associated with the obscuring torus around the nucleus. In Table 2, we show the offset of the S1 source from the UV peak, taken from the absolute astrometric result of Capetti et al. (1997). In Figure 14, the 5 GHz MERLIN radio map by Muxlow et al. (1996) is registered on the sharp UV image (F253M filter, fine focus), using this astrometric result. The uncertainty of the registration is indicated at the S1 source. Our new location of the nucleus is shown with the error stated in Table 2. The new location coincides with the S1 source within the errors. Therefore our result supports that the hidden nucleus resides in the S1 source.

7.2. *Three-dimensional Distribution*

The largest source of ambiguity in the derived three-dimensional distribution is the assumption of scattered-light domination in the UV range. Both of the two observational results described in § 6.1 are for large apertures and our assumption may not be valid especially in the faint regions.

We can roughly check this scattered-light domination by looking at the radial dependence of the UV flux in Figure 13. If we assume that the gas density, volume, and viewing angle are the same for all the clumps, the plotted points should distribute with a slope of −2. The overall distribution mostly follows this slope. However, some of the clumps are above the line. This could be compensated by the differences in density and volume, but it also would suggest the existence of diluting radiation (nonscattered, unpolarized light) in these clouds.

The determination of the viewing angle of the UV brightest cloud (UV peak) could be beyond the limit of our method, since the cloud is too close to the nucleus. In this case, inhomogeneity of the cloud within the aperture will

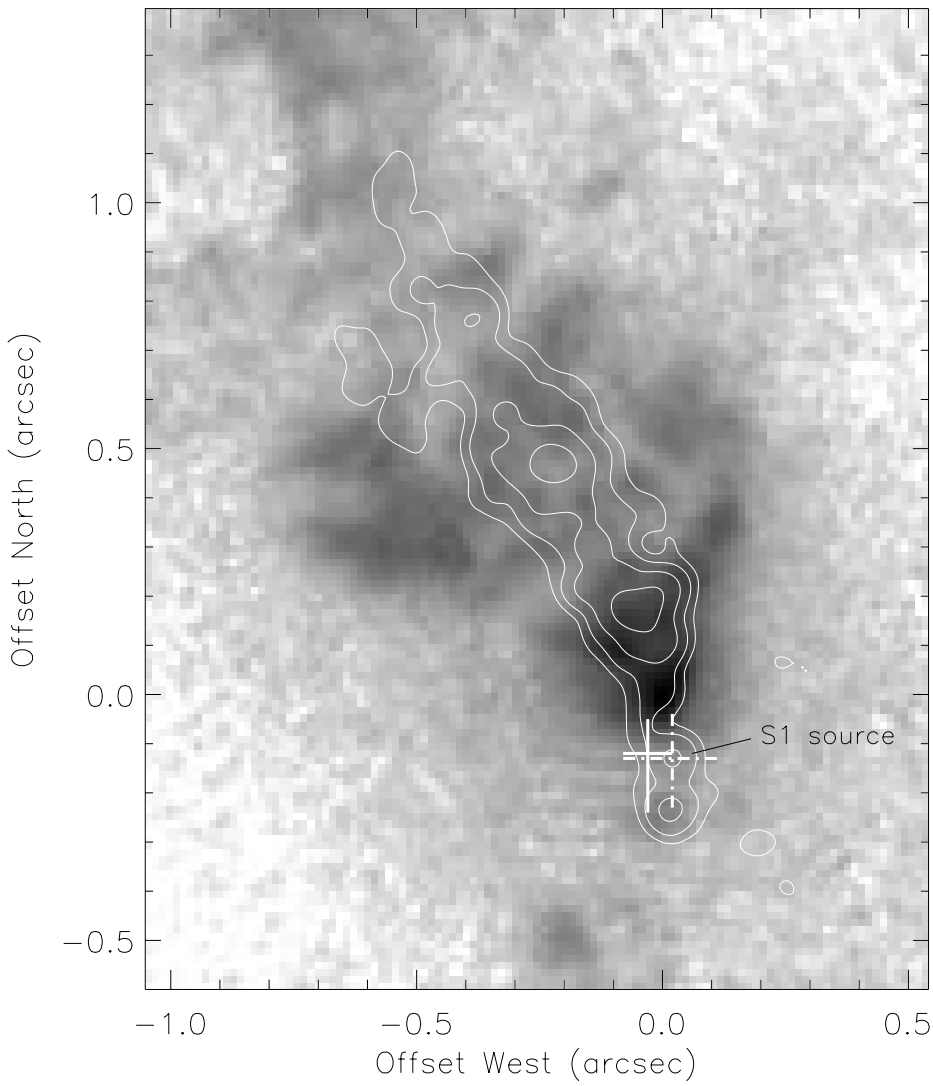

FIG. 14.—Registration of the 5 GHz MERLIN radio map (Muxlow et al. 1996) onto the *HST* sharp UV image, using the astrometric result of Capetti et al. (1997). Both are in log scale. The registration uncertainty is shown as a dash-dotted plus at the S1 source. Our new location of the nucleus is drawn as a solid plus, whose size represents our estimated error.

have a significant effect on the polarization, while these imaging polarimetry data do not have enough spatial resolution for further investigation. This uncertainty, however, does not affect the overall three-dimensional distribution in Figure 12.

A correlation between the optical morphology in the *HST* images and the radio jet structure (Muxlow et al. 1996; Gallimore et al. 1996a, 1996c; see Fig. 14) has been suggested by Capetti et al. (1997). Our three-dimensional distribution obtained might indicate a certain linear structure, which could be related to the jet structure. However, much more detailed consideration of the nature of the UV radiation is needed. Detailed analysis using other *HST* images, including the discussion of the fraction of diluting radiation, will be presented in a subsequent paper (Kishimoto 1999).

8. CONCLUSIONS

We have analyzed the *HST*/FOC imaging polarimetry data of NGC 1068 and shown that the data are consistent with a simple point-source scattering model, within the FOC polarimetric accuracy. We have redetermined the location of the nucleus by eliminating the regions that are suspected to have significant contaminations from the neighboring pixels. The error circle suggests that the nucleus is located between clouds A and B, and the most probable location of the nucleus has been found to be very close to cloud B, as close as $\sim 0\farcs08$, which is much closer than has ever been claimed before.

Based on this result, we have derived the three-dimensional view of the nuclear gas distribution, assuming that the UV radiation is dominated by scattered radiation in the bright knots. The inferred three-dimensional distribution of the clouds might suggest the existence of a linear structure that could be related to the radio jet, although the assumption of scattered-light domination should be examined using other high-resolution images.

The author thanks Robert Jedrzejewski for providing various information on the FOC polarimetry, and Robert Antonucci for his helpful suggestions to improve the manuscript. The author would like to thank Ryuko Hirata for his kind advice and generous support. The author also appreciates discussions with David Axon and Alessandro Capetti, and would like to thank Jack Gallimore for kindly providing the electronic data for the MERLIN radio map.

APPENDIX

ERROR ESTIMATION

In this appendix we summarize the method for the error estimation discussed in § 3.

Consider the incident radiation of the Stokes parameters (I, Q, U, V). The flux through three polarizers, $f_i (i = 1, 2, 3)$, is written as

$$f_i = \frac{1}{2} t_i [I - (k_i \cos 2\theta_i) Q - (k_i \sin 2\theta_i) U] , \tag{A1}$$

where t_i, k_i, and θ_i are each polarizer's transmittance, polarization efficiency, and axis direction, respectively. We define the polarizers' axis directions to be measured counterclockwise from the $+x$ axis direction of the image, while we set the reference plane of the Stokes parameter along the y axis so that the position angle of the polarization is measured counterclockwise from the y direction.

The Stokes parameters (I, Q, U) are derived from the observed fluxes f_i through each polarizer by the inverse relation of the above equation. For convenience, we define

$$f'_i \equiv \frac{2}{t_i} f_i , \tag{A2}$$

which corresponds to the transmittance-corrected incident flux for unpolarized light. If we write (I, Q, U) also as (I_1, I_2, I_3), these are calculated as

$$I_i = \sum_{j=1}^{3} a_{ij} f'_j , \tag{A3}$$

where

$$\begin{bmatrix} a_{11} & a_{12} & a_{13} \\ a_{21} & a_{22} & a_{23} \\ a_{31} & a_{32} & a_{33} \end{bmatrix} = \frac{1}{A} \begin{bmatrix} k_2 k_3 \sin(-2\theta_2 + 2\theta_3) \\ -k_2 \sin 2\theta_2 + k_3 \sin 2\theta_3 \\ k_2 \cos 2\theta_2 - k_3 \cos 2\theta_3 \end{bmatrix} \begin{bmatrix} k_3 k_1 \sin(-2\theta_3 + 2\theta_1) \\ -k_3 \sin 2\theta_3 + k_1 \sin 2\theta_1 \\ k_3 \cos 2\theta_3 - k_1 \cos 2\theta_1 \end{bmatrix} \begin{bmatrix} k_1 k_2 \sin(-2\theta_1 + 2\theta_2) \\ -k_1 \sin 2\theta_1 + k_2 \sin 2\theta_2 \\ k_1 \cos 2\theta_1 - k_2 \cos 2\theta_2 \end{bmatrix} , \tag{A4}$$

and

$$A = k_2 k_3 \sin(-2\theta_2 + 2\theta_3) + k_3 k_1 \sin(-2\theta_3 + 2\theta_1) + k_1 k_2 \sin(-2\theta_1 + 2\theta_2) . \tag{A5}$$

Note that for the nominal case of $\theta_1 = 180°$, $\theta_2 = 60°$, $\theta_3 = 120°$, and $k_1 = k_2 = k_3 = 1$, this equation simply becomes

$$\begin{bmatrix} I_1 \\ I_2 \\ I_3 \end{bmatrix} = \frac{1}{3} \begin{bmatrix} 1 & 1 & 1 \\ -2 & 1 & 1 \\ 0 & -\sqrt{3} & \sqrt{3} \end{bmatrix} \begin{bmatrix} f'_1 \\ f'_2 \\ f'_3 \end{bmatrix} . \tag{A6}$$

For the FOC polarizers at the transmission range of F253M filter, we take the polarization efficiencies to be (Nota et al. 1996, p. 38),

$$k_1 = 0.986, \quad k_2 = 0.976, \quad k_3 = 0.973 . \tag{A7}$$

The polarization degree P and position angle $\theta_{\rm PA}$ are calculated from I, Q, U as

$$P = \frac{\sqrt{Q^2 + U^2}}{I} ,$$

$$\theta_{\rm PA} = \frac{1}{2} \arctan \frac{U}{Q} . \tag{A8}$$

Now we estimate the total error in P with the following four major sources:

$$\sigma_P^2 = (\sigma_P^{\rm stat})^2 + (\sigma_P^{\rm shift})^2 + (\sigma_P^{\rm axis})^2 + (\sigma_P^{\rm corr})^2 . \tag{A9}$$

The statistical error in the photon counts $\sigma_P^{\rm stat}$ is a random error, while the other three errors, each described below, would be systematic errors. We treat these three, however, in the same way as we treat random errors, since we do not have enough calibration results to correct for them exactly.

The error from the image registration uncertainties $\sigma_P^{\rm shift}$ is estimated by actually shifting the images with the calibration uncertainties of 0.3 pixel (Hodge 1995) and calculating the resulting change of P. The other errors are calculated using equations (A2)–(A8) in the following way.

The statistical error $\sigma_P^{\rm stat}$ is written as

$$(\sigma_P^{\rm stat})^2 = \sum_{i=1}^{3} \left(\frac{\partial P}{\partial f_i} \right)^2 \sigma_{f_i}^2 , \tag{A10}$$

where σ_{f_i} is calculated assuming Poisson noise in the counts. The error from the uncertainties in the directions of polarizers' axes $\sigma_P^{\rm axis}$ is calculated as

$$(\sigma_P^{\rm axis})^2 = \sum_{i=1}^{3} \left(\frac{\partial P}{\partial \theta_i} \right)^2 \sigma_{\theta_i}^2 , \tag{A11}$$

where we take σ_{θ_i} to be 3° (Nota et al. 1996, p. 36; see also Robinson & Thomson 1995). Finally, $\sigma_P^{\rm corr}$ is the error from the uncertainties in the correction factors, discussed in § 3, to be multiplied to each of f_i. To take this into account, we rewrite f'_i to define correction factors ξ_i as

$$f'_i = \xi_i \frac{2}{t_i} f_i \tag{A12}$$

and derive $\sigma_P^{\rm corr}$ from

$$(\sigma_P^{\rm corr})^2 = \sum_{i=1}^{3} \left(\frac{\partial P}{\partial \xi_i} \right)^2 \sigma_{\xi_i}^2 , \tag{A13}$$

where we take σ_{ξ_i} at most to be 0.05 for cases A and C, 0.04 for case B, estimating from three kinds of uncertainties discussed in § 3. All partial derivatives can be calculated from equations (A2)–(A8) and (A12), setting $\theta_1 = 180°$, $\theta_2 = 60°$, $\theta_3 = 120°$, and $\xi_i = 1$.

The error in $\theta_{\rm PA}$ can also be estimated in just the same manner as σ_P above. The well-known approximate relation in high S/N case,

$$\sigma_{\theta_{\rm PA}} \simeq \frac{1}{2} \frac{\sigma_P}{P} \qquad \text{(in radians)} , \tag{A14}$$

holds only for $\sigma_P^{\rm stat}$ and $\sigma_P^{\rm corr}$ (note the similarity between $\partial P/\partial f_i$ and $\partial P/\partial \xi_i$), but not for $\sigma_P^{\rm shift}$ nor $\sigma_P^{\rm axis}$. In particular, $\sigma_{\theta_{\rm PA}}^{\rm axis}$ simply becomes

$$\sigma_{\theta_{\rm PA}}^{\rm axis} = \frac{1}{\sqrt{2}} \sigma_\theta \tag{A15}$$

when we set the uncertainty in all the three polarizers' axes to be σ_θ and all three polarization efficiencies to be the same.

REFERENCES

Antonucci, R., Hurt, T., & Miller, J. S. 1994, ApJ, 430, 210
Antonucci, R., & Miller, J. S. 1985, ApJ, 297, 621
Bland-Hawthorn, J., Gallimore, J. F., Tacconi, L. J., Brinks, E., Baum, S. A., Antonucci, R. R. J., & Cecil, G. N. 1997, Ap&SS, 248, 9
Braatz, J. A., Wilson, A. S., Gezari, D. Y., Varosi, F., & Beichman, C. A. 1993, ApJ, 409, L5
Brown, J. C., & McLean, I. S. 1977, A&A, 57, 141
Capetti, A., Axon, D. J., Macchetto, F., Sparks, W. B., & Boksenberg, A. 1995a, ApJ, 446, 155
Capetti, A., Macchetto, F., Axon, D. J., Sparks, W. B., & Boksenberg, A. 1995b, ApJ, 452, L87
Capetti, A., Macchetto, F., & Lattanzi, M. G. 1997, ApJ, 476, L67
Evans, I. N., Ford, H. C., Kinney, A. L., Antonucci, R. R. J., Armus, L., & Caganoff, S. 1991, ApJ, 369, L27
Gallimore, J. F., Baum, S. A., & O'Dea, C. P. 1996a, ApJ, 464, 198
Gallimore, J. F., Baum, S. A., O'Dea, C. P., Brinks, E., & Pedlar, A. 1994, ApJ, 422, L13
———. 1996b, ApJ, 462, 740
Gallimore, J. F., Baum, S. A., O'Dea, C. P., & Pedlar, A. 1996c, ApJ, 458, 136
Greenhill, L. J., & Gwinn, C. R. 1997, Ap&SS, 248, 261
Greenhill, L. J., Gwinn, C. R., Antonucci, R., & Barvainis, R. 1996, ApJ, 472, L21
Hodge, P. E. 1993, FOC Instrument Science Report, 69
———. 1995, FOC Instrument Science Report, 89
Kishimoto, M. 1997, Ap&SS, 248, 277
———. 1999, in preparation
Krist, J. 1993, in ASP Conf. Ser. 52, Astronomical Data Analysis Software and Systems II, ed. R. J. Hanisch, R. J. V. Brissenden, & J. Barnes (San Francisco: ASP), 530
Macchetto, F., Capetti, A., Sparks, W. B., Axon, D. J., & Boksenberg, A. 1994, ApJ, 435, L15
Miller, J. S., Goodrich, R. W., & Mathews, W. G. 1991, ApJ, 378, 47
Muxlow, T. W. B., Pedlar, A., Holloway, A. J., Gallimore, J. F., & Antonucci, R. R. J. 1996, MNRAS, 278, 854
Nota, A., et al. 1996, FOC Instrument Handbook Version 7.0 (Baltimore: STScI)
Robinson, D. R. T., & Thomson, R. C. 1995, in Calibrating *HST*: Post Servicing Mission, ed. A. Koratkar & C. Leitherer (Baltimore: STScI)
Simmons, J. F. L., & Stewart, B. G. 1985, A&A, 142, 100
Thatte, N., Quirrenbach, A., Genzel, R., Maiolino, R., & Tecza, M. 1997, ApJ, 490, 238
Tran, H. D. 1995a, ApJ, 440, 565
———. 1995b, ApJ, 440, 578
———. 1995c, ApJ, 440, 597
Tully, R. B. 1988, Nearby Galaxies Catalog (Cambridge: Cambridge Univ. Press)
Wardle, J. F. C., & Kronberg, P. P. 1974, ApJ, 194, 249
Young, S., Packham, C., Hough, J. H., & Efstathiou, A. 1996, MNRAS, 283, L1